International Journal of Minerals, Metallurgy and Materials
Volume 30, Number 4, April 2023, Page 734
https://doi.org/10.1007/s12613-022-2531-3

Hot deformation behavior of Fe–27.34Mn–8.63Al–1.03C lightweight steel

Haitao Lu, Dazhao Li✉*, Siyuan Li, and Yong'an Chen*

School of Materials Science and Engineering, North University of China, Taiyuan 030051, China
(Received: 20 January 2022; revised: 3 August 2022; accepted: 4 August 2022)

Abstract: Hot compression tests were performed to investigate the hot deformation behavior of Fe–27.34Mn–8.63Al–1.03C lightweight steel and optimize the hot workability parameters. The temperature range was 900–1150°C and the strain rate range was 0.01–5 s^{-1} on a Gleeble-3800 thermal simulator machine. The results showed that the flow stress increased with decreasing deformation temperature and increasing strain rate. According to the constitutive equation, the activation energy of hot deformation was 422.88 kJ·mol^{-1}. The relationship between the critical stress and peak stress of the tested steel was established, and a dynamic recrystallization kinetic model was thus obtained. Based on this model, the effects of strain rate and deformation temperature on the volume fraction of dynamically recrystallized grains were explored. The microstructural examination and processing map results revealed that the tested steel exhibited a good hot workability at deformation temperatures of 1010–1100°C and strain rate of 0.01 s^{-1}.

Keywords: Fe–Mn–Al–C steel; hot deformation; activation energy; microstructural evolution; processing map

1. Introduction

The increasing demand for energy savings and emission reductions has made lightweight vehicle bodies a development direction in the automobile industry. As a result, an increasing number of researchers have focused on Fe–Mn–Al–C lightweight steel materials, which can be classified into four categories based on their alloy content: ferritic, ferrite-based duplex, austenite-based duplex, and austenitic steels [1–6]. Compared to traditional automotive steels [7–11], the density of Fe–Mn–Al–C steel is 10%–20% lower while still offering strain-strengthening characteristics under the collective effect of various alloys [12–17]. The deformation mechanism suggests that the presence of nano-sized κ-carbides in the Fe–Mn–Al–C steel matrix induces the microband-induced plasticity mechanism, which can coordinate the deformation degree of different parts and significantly improve steel plasticity [18–21].

Dynamic recrystallization occurs when the original coarse grains are replaced by new homogeneously distributed refined grains during hot deformation of steels, thus eliminating defects in the grains [22–24]. The resulting homogeneous microstructure restrains the occurrence of flow instability and effectively enhances the hot workability. Therefore, it is essential to study the dynamic recrystallization behavior during hot deformation. Several scholars have evaluated the hot deformation behavior and hot workability of Fe–Mn–Al–C steel. Xu *et al.* [25] studied the hot deformation behavior of Fe–26Mn–6.2Al duplex steel and pointed out that the recrystallization behavior of δ-ferrite prior to austenite resulted in abnormal behavior of the flow curves. Liu *et al.* [26] analyzed two characteristic flow behaviors and dynamic recrystallization behaviors of multiphase Fe–11Mn–10Al–0.9C steel. They found that the deformation-induced α-ferrite could slow down austenite recrystallization through the pinning effect and refine the austenite grain size. There are also some differences between austenitic steel and duplex steel. Pierce *et al.* [27] discussed the hot deformation behavior of austenitic steel with a large grain size. They reported that the large grains did not provide sufficient nucleation sites, thus resulting in changes in the conditions that drive dynamic recrystallization. Hamada *et al.* [18] showed that the newly recrystallized austenite had a "necklace" structure distributed in the original austenite grain boundaries at a low deformation temperature and a high strain rate. This abnormal structure can easily lead to flow instability. However, there is still limited insight on the hot deformation behavior of hot-rolled Fe–Mn–Al–C steels. The effects of dynamic recrystallization behavior on the flow stability and hot workability are unclear.

Here, a uniaxial hot compression experiment was performed on Fe–27.34Mn–8.63Al–1.03C lightweight steel. To study the deformation behavior of the tested steel before and after dynamic recrystallization, the deformation temperature ranged from 900 to 1150°C. The stress–strain response of the tested steel under static and dynamic deformation conditions was explored, and the strain rate ranged from 0.01 to 5 s^{-1}. A constitutive equation and dynamic recrystallization model were established based on the flow stress analysis. After analyzing the microstructure and processing map, the effect of

✉ Corresponding author: Dazhao Li E-mail: lidazhao@nuc.edu.cn, dazhaoli@163.com

deformation temperature and strain rate on the deformation structure was clarified. Finally, the relationship between peak stress and critical stress was obtained.

2. Experimental

The tested steel was smelted in a 50-kg vacuum induction smelting furnace and its chemical composition is presented in Table 1. The as-cast specimens were hot-rolled at temperatures ranging from 1000 to 1100°C with a final thickness of 30 mm. After rolling, hot compression specimens were prepared with dimensions of ϕ10 mm × 15 mm. The density of the tested steel was measured multiple times according to the drainage method, and the average density value was 6.77 g·cm^{-3}.

Table 1. Chemical composition of the tested steel wt%

Mn	Al	C	Si	P	S	Fe
27.34	8.63	1.03	0.24	0.017	0.001	Bal.

A Gleeble-3800 thermal simulation machine was used to heat the samples to 1200°C at 10°C·s^{-1} and the temperature was held for 180 s. They were then cooled to the relevant deformation temperatures (1150, 1100, 1050, 1000, 950, and 900°C) at a rate of 10°C·s^{-1}. The strain rates were 0.01, 0.1, 1, and 5 s^{-1}, and the maximum true strain was 0.7. After deformation, the specimens were quenched to room temperature within 5 s to retain the recrystallized structure. Fig. 1 shows the schematic of the hot compression simulation and the test process.

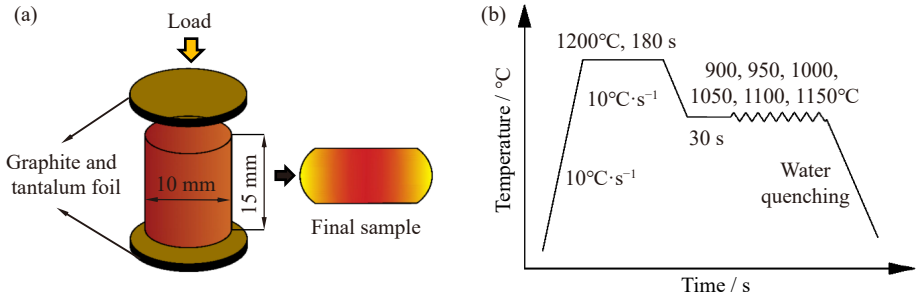

Fig. 1. Schematic diagram of (a) hot compression simulation and (b) test process.

Subsequently, the metallographic structures in the longitudinal section of the hot-compressed specimens were observed. After grinding and polishing, the section was corroded with 4% nital. The microstructures were observed with the Leica MI8 metallographic microscope. X-ray diffraction (XRD, Bruker D8 ADVANCE) was performed on the polished specimens. The scanning range was between 30° and 90° with a scanning speed of 2°·min^{-1}.

3. Results and discussion

3.1. Flow stress behaviour

The true stress–strain curves of the Fe–27.34Mn–8.63Al–1.03C lightweight steel at different temperatures and strain rates are shown in Fig. 2. At the same strain rates, the flow stress decreased with increasing deformation temperature. The range of flow stress gradually increased with increasing strain rate. Therefore, both the increasing deformation temperature and decreasing strain rate led to a decrease in flow stress. In other words, the flow stress is sensitive to deformation temperature and strain rate.

Fig. 2 depicts the true stress–strain curves for the tested steel, which shows significant characteristics of work-hardening and dynamic softening effects. However, it is clear that the flow stress in Fig. 2(c) and (d) fluctuates significantly compared to that in Fig. 2(a) and (b), which is related to the massive formation and multiplication of dislocations at high strain rate [28]. As the strain rate increases, there is an abnormal flow stress behavior due to blocking and entanglement of dislocations or due to interactions between dislocations and precipitation [21,28].

All of the stress–strain curves could be divided into three different stages. The deformation mechanism of the tested steel that occurred in stage I was dominated by work-hardening (Fig. 2(c)), which resulted in a rapid increase in true stress until the yield-point-elongation effect occurred [29]. This effect was prominent in curves with strain rates of 0.1 and 1 s^{-1} and deformation temperatures of 900, 950, and 1000°C, as shown by arrows in Fig. 2(b) and (c). Sun *et al.* [28] reported that the Cottrell atmosphere was formed by the segregation of interstitial C atom near the dislocation line. The firmly pinning effect between dislocations and C atoms limited the movement of dislocations, thus leading to a yield-point-elongation effect. The stress reached a peak value in stage II. However, the work-hardening effect still played a dominant role in this process and increased flow stress. Dynamic softening started to occur in stage III. The dynamic balance between work-hardening and dynamic softening effects contributed to steady stress–strain curves.

During the whole deformation stage, the deformation mechanism of the tested steel was determined by the interaction between work-hardening and dynamic softening effects. Meanwhile, the work-hardening effect was mainly related to dislocation migration [25]. The dynamic softening effect was primarily associated with dynamic recovery and dynamic recrystallization. At the initial deformation stage, the dislocations in the deformed grains began to slip and accumulate, thus contributing to the enhanced work-hardening. As the strain increased, the interaction between the work-hardening effect and the dynamic softening effect resulted in peak

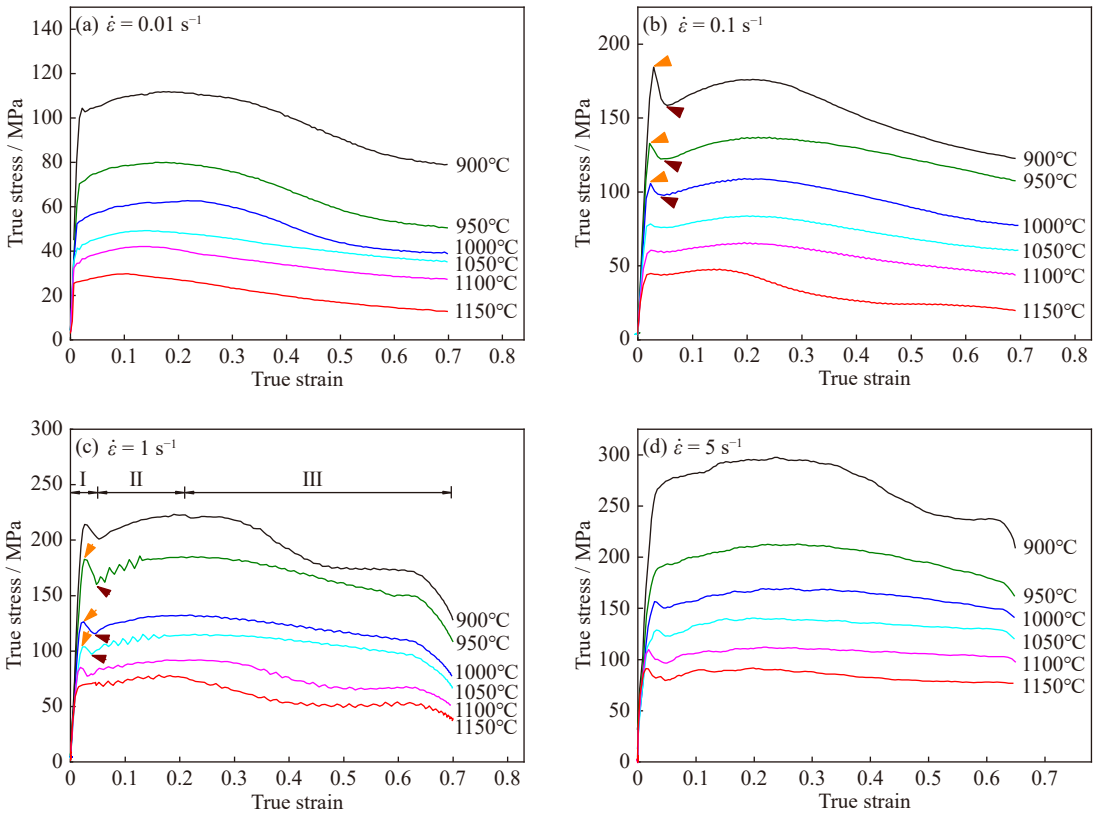

Fig. 2. True stress–strain curves at different strain rates ($\dot{\varepsilon}$): (a) 0.01 s^{-1}; (b) 0.1 s^{-1}; (c) 1 s^{-1}; (d) 5 s^{-1}.

stress. When dynamic recrystallization became the dominant deformation mechanism, there were a softening effect from the newly recrystallized grains with lower density dislocations and a work-hardening effect from the original grains with higher density dislocations. These two effects reached a dynamic balance, which made the flow stress of the tested steel reach a steady state [30].

3.2. Constitutive modeling

The constitutive equation is widely used for flow stress analysis because it directly reflects the effects of deformation temperature and strain rate on the flow stress. Eq. (1) shows the usual expression of the constitutive equation [31–32]:

$$Z = \dot{\varepsilon}\exp\left(\frac{Q}{RT}\right) \tag{1}$$

where Z is the Zener–Hollomon constant; $\dot{\varepsilon}$ is the strain rate (s^{-1}); Q is the activation energy (J·mol^{-1}); R is the gas constant (R = 8.314 J·mol^{-1}·K^{-1}), and T is the deformation temperature (K). Sellars and Tagert also suggested a method that can be applied to any stress state to avoid error, as expressed by Eqs. (2)–(3) [32–33]:

$$\dot{\varepsilon} = A\left[\sinh\left(\alpha\sigma_{\mathrm{p}}\right)\right]^{n}\exp\left(-\frac{Q}{RT}\right) \tag{2}$$

$$\ln\dot{\varepsilon} = \ln A + n\ln\left[\sinh\left(\alpha\sigma_{\mathrm{p}}\right)\right] - \frac{Q}{RT} \tag{3}$$

where σ_{p} is peak stress; A, n, and α are the material constants. Based on Fig. 3(a) and (b), the slopes after linear fitting are n_1 and β, respectively. Term α can then be defined as $\alpha = \beta/n_1 = 0.0107$, which is similar to that in the literature (Table 2). As mentioned above, α is related chiefly to σ_{p}. Therefore, the values of α vary with the elementary composition and the heat treatment process, but they all fluctuate within a reasonable range. When T and $\dot{\varepsilon}$ are constants, Eq. (3) can be written as Eqs. (4) and (5), respectively:

$$n = \left.\frac{\partial\ln\dot{\varepsilon}}{\partial\ln\left[\sinh\left(\alpha\sigma_{\mathrm{p}}\right)\right]}\right|_{T} \tag{4}$$

$$\begin{aligned} Q &= R\left\{\frac{\partial\ln\left[\sinh\left(\alpha\sigma_{\mathrm{p}}\right)\right]}{\partial(1/T)}\right\}_{\dot{\varepsilon}}\left\{\frac{\partial\ln\dot{\varepsilon}}{\partial\ln\left[\sinh\left(\alpha\sigma_{\mathrm{p}}\right)\right]}\right\}_{T} \\ &= Rn\left\{\frac{\partial\ln\left[\sinh\left(\alpha\sigma_{\mathrm{p}}\right)\right]}{\partial(1/T)}\right\}_{\dot{\varepsilon}} \end{aligned} \tag{5}$$

Eqs. (4) and (5) indicate that $\ln[\sinh(\alpha\sigma_{\mathrm{p}})]$ has a linear correlation with $\ln\dot{\varepsilon}$ and $1/T$, as shown in Fig. 3(c) and (d), the slopes are denoted as n and b, respectively. Term n is 4.2363, which is consistent with that in the literature (Table 2). Based on Eq. (5), the activation energy Q of hot deformation at various temperatures and strain rates can be obtained through $Q = R\times n\times b$. The average Q value is 422.88 kJ·mol^{-1}, which is reasonable when compared with values (290–470 kJ·mol^{-1}) in the literature (Table 2).

Generally, the activation energy of hot deformation is mainly influenced by elements addition, phase composition, and heat treatment. This indicates the deformation resistance of materials [27,36,39]. Many studies have been carried out to determine the influencing factors. Khosravifard *et al.* [36] examined the hot deformation process of as-cast steel with

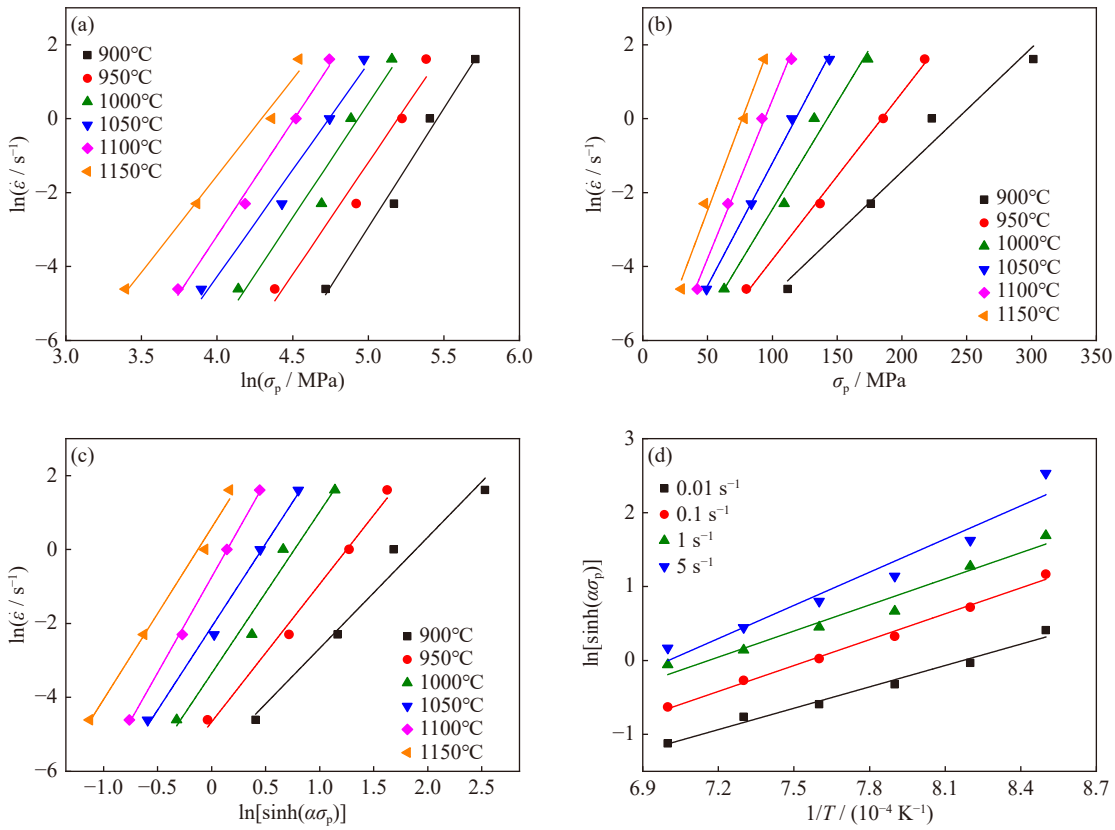

Fig. 3. Relationship between flow stress and strain rate of test steel: (a) ln$\dot{\varepsilon}$–lnσ_p; (b) ln$\dot{\varepsilon}$–σ_p; (c) ln$\dot{\varepsilon}$–ln[sinh($\alpha\sigma_p$)]; (d) ln[sinh($\alpha\sigma_p$)]–1/*T*.

Table 2. Data for phase composition, material constants (n, α), and activation energy of hot deformation for lightweight steels

Alloy	T / °C	$\dot{\varepsilon}$ / s^{-1}	Phase	n	α	Q / (kJ·mol^{-1})	Ref.
Fe–30Mn–9Al–1Si–0.9C–0.5Mo	1000–1200	0.1–7.8	γ + δ	4.95	0.007	470 ± 90	[27]
Fe–30Mn–10Al–1C	850–1150	0.01–10	γ	5.165	0.004	391.572	[28]
Fe–27Mn–11.5Al–0.95C	900–1150	0.01–10	γ + δ	3.9284	0.0035	294.204	[34]
Fe–21Mn–10Al–1.5C–2Si	900–1150	0.01–1	γ	4.8019	0.004	293	[35]
Fe–20.1Mn–2.1Si–0.6Al–0.07C	900–1100	0.01–10	—	—	—	411	[36]
Fe–21.6Mn–2.7Si–0.8Al–0.49C	900–1100	0.01–10	—	—	—	429	[36]
Fe–25Mn–3Al	900–1100	0.005–5	γ	—	—	397	[37]
Fe–25Mn–6Al	900–1100	0.005–0.5	γ	—	—	405	[18]
Fe–25Mn–8Al	900–1100	0.005–0.5	γ + δ	—	—	300	[18]
Fe–26Mn–8Al–1C	850–1150	0.001–10	γ	4.9383	0.006	394	[38]
Fe–26Mn–10Al–1C	850–1150	0.001–10	γ + δ	1.9048	0.0125	443	[38]
Fe–27.34Mn–8.63Al–1.03C	900–1150	0.01–5	γ	4.2363	0.0107	422.88	This work

different C contents. They found that the activation energy (411 kJ·mol^{-1}) of low carbon steel was slightly lower than that (429 kJ·mol^{-1}) of high carbon steel. The hot deformation activation energy thus increases with increasing C content.

Hamada *et al.* [18,37] investigated the effect of various Al contents on the activation energies of hot deformation for Fe–25Mn–*x*Al–0.1C steel (x = 3, 6, and 8). They indicated that the activation energy increased from 397 kJ·mol^{-1} for 3Al steel to 405 kJ·mol^{-1} for 6Al steel, but it decreased to 300 kJ·mol^{-1} for 8Al steel. This is because the matrix phase changed from single austenite for 3Al and 6Al steels to dual-phase (austenite and ferrite) for 8Al steel. The hot deformation activation energy of austenitic steels is thus higher than that of duplex steels (austenite and ferrite). However, Wu *et al.* [38] suggested that the hot deformation activation energy of duplex steel (austenite and ferrite) was higher than that of austenitic steel, as shown in Table 2.

The analysis indicates that hot deformation activation energy of steels is closely related to the phase composition. In austenite steels, the hot deformation activation energies are strongly affected by the austenite grain size and κ-carbide precipitation. Pierce *et al.* [27] noted that the hot deformation activation energy of austenite with large grains was higher than that of austenite with small grains. Zambrano *et al.* [35] noted that the formation of κ-carbide precipitation in austenitic steels could reduce the activation energy during hot de-

formation. In duplex steels (austenite and ferrite), the inhomogeneous strain distribution between hard austenite and soft ferrite could affect the flow stress and activation energy [25,34]. However, few studies have reported the effect of phase volume fraction in duplex steels on the hot deformation activation energy. This needs to be further confirmed in future work.

Eq. (6) can be obtained based on Eqs. (1) and (2). Fig. 4 shows the ln$A$ is the intercept of the ln$Z$–ln[sinh($\alpha\sigma_p$)] curve, which is calculated as 36.37. The fitted results in Fig. 4 showed that the linear correlation coefficient (R^2) was 0.97 thus indicating that parameter Z well represents the flow stress. Then the Z equation was obtained as follows:

$$\ln Z = \ln A + n\ln\left[\sinh\left(\alpha\sigma_p\right)\right] \tag{6}$$

$$Z = \dot{\varepsilon}\exp\left(\frac{422880}{RT}\right) = 6.239\times10^{15}\left[\sinh\left(0.0107\sigma_p\right)\right]^{4.24} \tag{7}$$

3.3. Critical condition for dynamic recrystallization

The critical stress σ_c is the basis for investigating the dynamic recrystallization of austenite—this can be obtained by the work hardening rate (WHR, $\theta = d\sigma/d\varepsilon$) curve [40]. σ and ε represent the true stress and true strain at different deformation temperatures and strain rates. The curves of θ–ε and ($d\theta/d\varepsilon$)–ε for test steel at a strain rate of 0.01 s^{-1} and various temperatures showed a similar trend (Fig. 5). According to the "double differential method" criterion [34,41], the critical strain can be found based on Fig. 5.

The critical stress σ_c at different temperatures and strain rates could be acquired, and it gradually decreased with an increase in hot deformation temperature and a decrease in strain rate (Table 3). As the hot deformation temperature increased, a softening effect occurred and the dislocation density decreased, weakening the work-hardening effect. In turn, the critical stress decreased. Mandal *et al.* [42] found that the initial critical dislocation density for dynamic recrystallization at a certain temperature dropped with the decreasing strain rate. The relationship between peak stress (σ_p)–peak strain (ε_p) and critical stress (σ_c)–critical strain (ε_c) could be obtained through the linear fitting of the relevant data in Fig. 6. All of the parameters are shown in Eqs. (8)–(11):

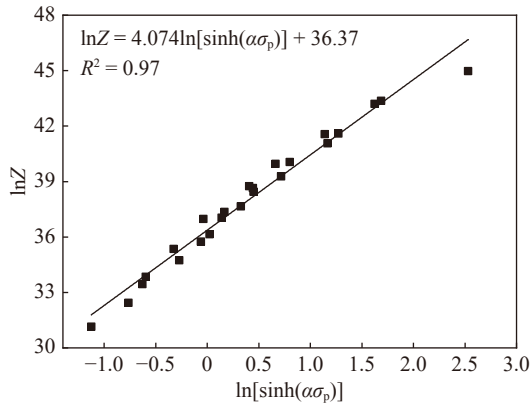

Fig. 4. Relationship of ln$Z$ and ln[sinh($\alpha\sigma_p$)].

$$\sigma_p = 0.237Z^{0.16} \tag{8}$$

$$\sigma_c = 0.214Z^{0.159} \tag{9}$$

$$\varepsilon_c = 4.6\times10^{-3}Z^{0.05} \tag{10}$$

$$\sigma_c = 0.872\sigma_p \tag{11}$$

According to Eqs. (9) and (10), the Z parameter of the tested steel changed exponentially with critical stress and strain. A larger Z value implied a greater critical stress for dynamic recrystallization. Meanwhile, the corresponding critical strain would increase accordingly. Moreover, the occurrence of dynamic recrystallization strongly depended on the

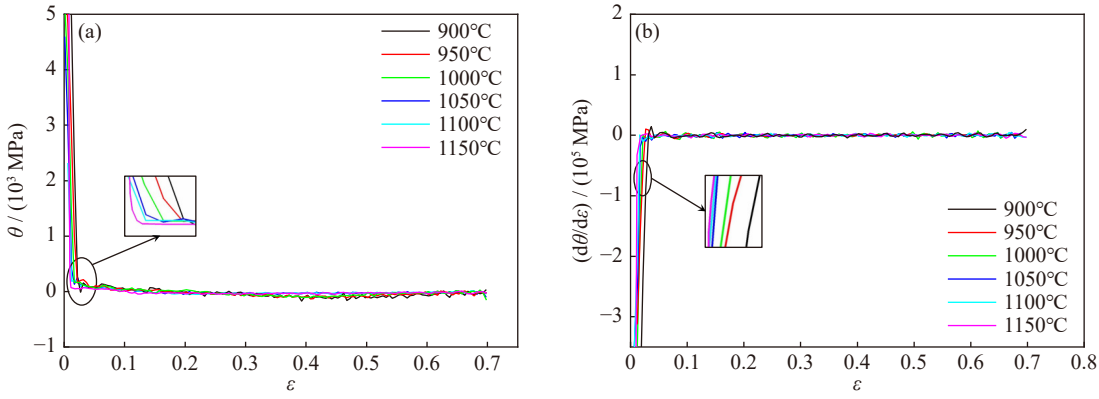

Fig. 5. The WHR curves at $\dot{\varepsilon}$ = 0.01 s^{-1}: (a) θ–ε; (b) ($d\theta/d\varepsilon$)–ε.

Table 3. Critical stress (σ_c) values under different deformation conditions MPa

$\dot{\varepsilon}$ / s^{-1}	T / °C					
	900	950	1000	1050	1100	1150
0.01	107.99	71.91	53.98	42.95	34.64	26.33
0.1	163.17	124	98.47	76.38	59.48	44.36
1	200.99	160.11	115.62	97.27	77.2	70.27
5	264.63	182.18	150.39	116.54	98.79	81.98

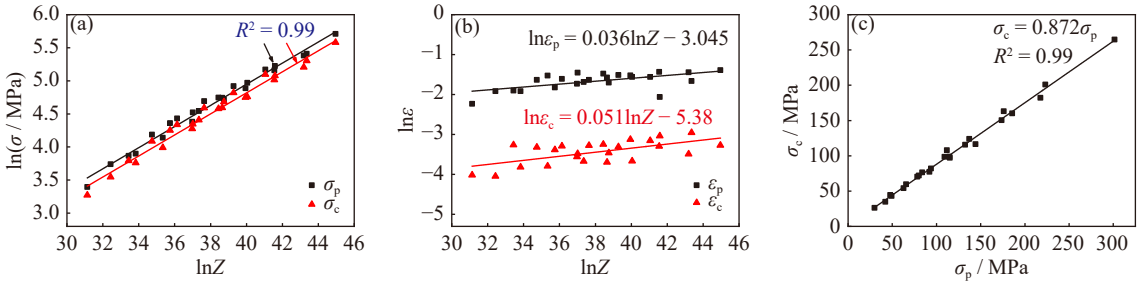

Fig. 6. Relationship of (a) lnσ_p, lnσ_c, and ln$Z$; (b) lnε_p, lnε_c, and ln$Z$; (c) σ_p and σ_c.

deformation conditions. More strain variables were required to drive the recrystallization process under a lower deformation temperature and a higher strain rate.

3.4. Dynamic recrystallization kinetic

The dynamic recrystallization volume fraction reflects the degree of dynamic recrystallization during hot deformation of the tested steel; thus, it is necessary to establish a dynamic recrystallization dynamic model to characterize the process. In this study, the matrix phase of the tested steel was austenite, and the dynamic recrystallization volume fraction of austenite (X) was calculated according to Eq. (12) [34,43]:

$$X = \frac{\sigma_p - \sigma}{\sigma_p - \sigma_s} \tag{12}$$

where σ_p is the peak stress, σ_s is the steady state stress, and σ is true stress at different temperatures and strain rates, which can be obtained from the stress–strain curves. On the basis of previous studies [44–45], Eq. (12) could also be expressed as Eq. (13):

$$X = 1 - \exp\left[-k\left(\frac{\varepsilon - \varepsilon_c}{\varepsilon_p}\right)^u\right] \tag{13}$$

where ε_p is the peak strain, ε_c is critical strain, and ε is the true strain. The values of k and u were obtained by determining the relationship between ln{ln[1/(1−X)]} and ln[(ε−ε_c)/ε_p], as shown in Fig. 7. Therefore, the dynamic recrystallization kinetics model of the tested steel could be obtained as follows:

$$X = 1 - \exp\left[-0.0467\left(\frac{\varepsilon - \varepsilon_c}{\varepsilon_p}\right)^{3.923}\right] \tag{14}$$

Based on Eq. (14), the volume fraction of dynamic recrystallized grain of the tested steel can be calculated as shown in Fig. 8.

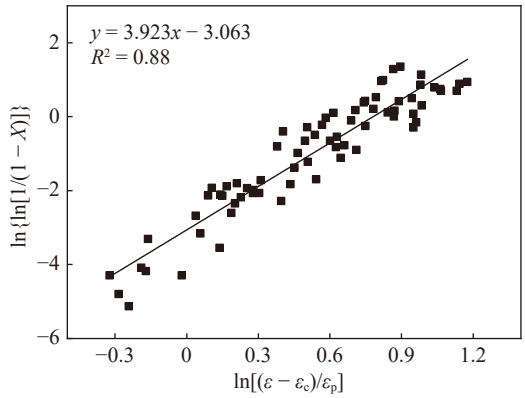

Fig. 7. Relationship between ln[(ε−ε_c)/ε_p] and ln{ln[1/(1−X)]} under various deformation conditions.

Fig. 8 shows that the dynamic recrystallization curves present an "S" shape at different deformation temperatures and strain rates. The volume fraction of dynamic recrystallization grains increases with increasing strain. This suggests that the volume fraction of dynamically recrystallized grains increased with increasing temperature and strain (Fig. 8(a)). An increase in deformation temperature can accelerate the migration speed of the grain boundaries, dislocations, and other defects. This in turn promotes dynamic recrystallization. Fig. 8(b) shows that the volume fraction of dynamic recrystallization grains decreased with increasing strain rate at the same deformation temperature. This is because a low strain rate can provide sufficient time for dynamic recrystal-

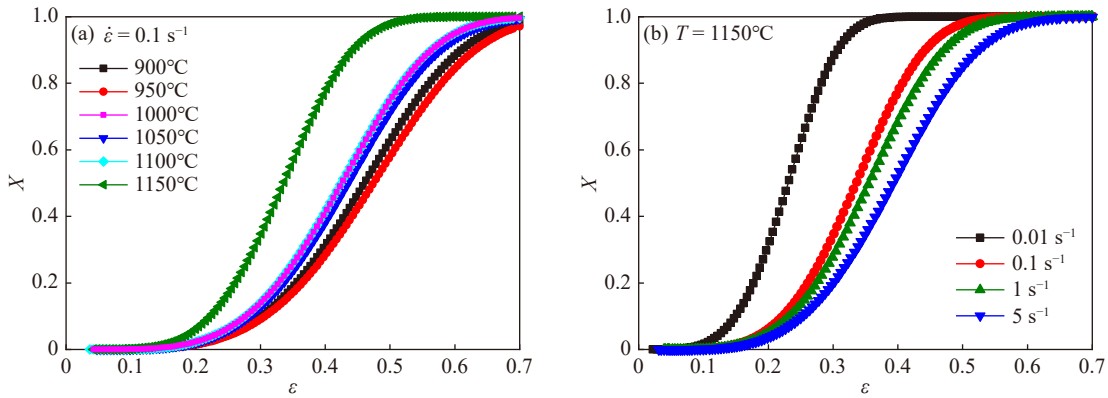

Fig. 8. Predicted results of the volume fraction of dynamic recrystallization grains under various deformation conditions: (a) 0.1 s^{-1}; (b) 1150°C.

lization. Therefore, a high temperature and a low strain rate can provide a suitable condition for dynamic recrystallization to obtain a more homogeneous structure.

3.5. Microstructure evolution

The hot compression deformation behavior of the tested steel is affected by the microstructure evolution. Fig. 9(a)–(f) shows the microstructures of the tested steel at different deformation temperatures and strain rates. The data combined with the XRD patterns in Fig. 10 suggested that austenite was the matrix phase. Additionally, the newly refined austenite recrystallized grains arched and nucleated at the original elongated austenite grain boundaries.

The volume fraction of recrystallized austenite grains decreased with increasing strain rate at a constant deformation temperature. When the strain rate was 0.01 s^{-1}, many recrystallized austenite grains gathered near the original austenite grain boundary, as shown in Fig. 9(a). The dynamic recrystallization was weakened when the strain rate increased to 5 s^{-1}. The volume fraction of recrystallized grains in Fig. 9(c) decreased significantly compared to that in Fig. 9(a) and (b). This is because the stored deformation energy could not provide enough driving force for austenite recrystallization at low strain rates. This leads to a reduced nucleation rate. However, the recrystallized grains have enough time to grow. In contrast, the defects in austenite increase the stored energy at high strain rates. Unfortunately, the dynamic recovery does not have enough time to eliminate the defects. Therefore, the recrystallized grains nucleate near the defects, but the grain size still remains small.

Fig. 9(d)–(f) shows the microstructures of the tested steel at different deformation temperatures (950, 1050, and 1150°C) with the same strain rate of 0.1 s^{-1}. With an increase in deformation temperature, the original austenite grains were gradually replaced by newly refined equiaxed grains, implying that the recrystallization fraction of austenite increased. At 950°C, a low deformation temperature could not provide enough atomic diffusion capacity and sufficient recrystallization driving force, thus resulting in a small number of recrystallized grains distributed at the original grain boundaries in a "necklace" structure (Fig. 9(d)). The dynamic recrystallization process was complete as the deformation temper-

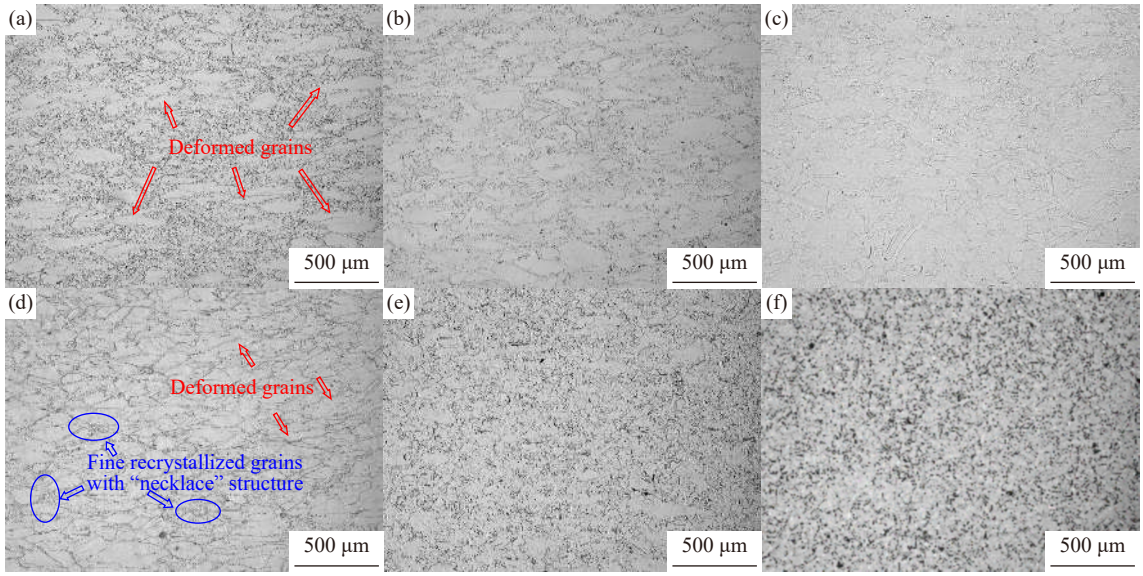

Fig. 9. Metallographic microstructure under different deformation conditions: (a) 1000°C, 0.01 s^{-1}; (b) 1000°C, 0.1 s^{-1}; (c) 1000°C, 5 s^{-1}; (d) 950°C, 0.1 s^{-1}; (e) 1050°C, 0.1 s^{-1}; (f) 1150°C, 0.1 s^{-1}.

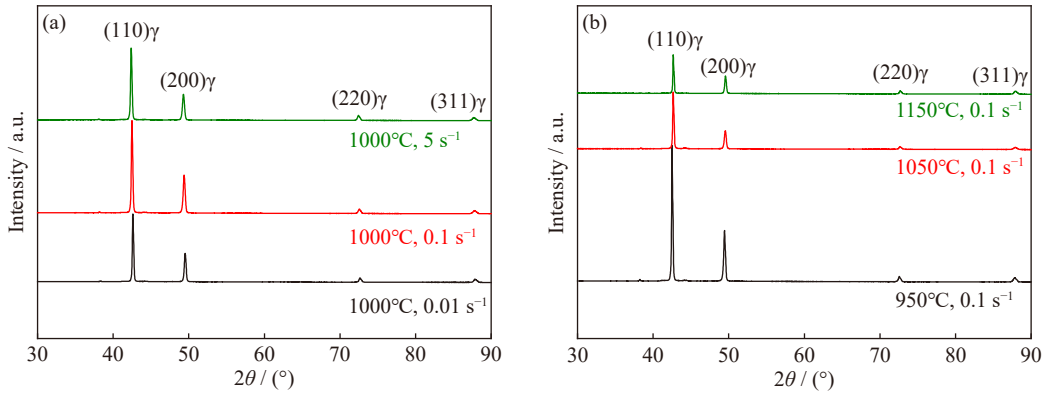

Fig. 10. XRD patterns of the tested steel under different deformation conditions: (a) 1000°C, 0.01, 0.1, and 5 s^{-1} and (b) 0.1 s^{-1}, 950, 1050, and 1150°C.

ature increased to 1050°C (Fig. 9(e)). In other words, the original austenite grains were entirely replaced by refined recrystallized grains. This is because a higher deformation temperature promotes the movement of dislocations and increases the nucleation rate, which benefits dynamic recrystallization. The recrystallized austenite grain size significantly increased when the deformation temperature increased to 1150°C (Fig. 9(f)).

3.6. Processing map

Processing map are widely used to evaluate material machinability. Prasad *et al.* [46–47] proposed a dynamic material model (DMM) to construct a processing map and optimize the hot working process by analyzing and predicting the deformation behavior of materials under various conditions. The processing map for the tested steel under different deformation temperatures and strain rates was thus constructed.

The total energy P of the tested steel during the hot deformation can be converted into two parts based on the DMM theory: the energy G consumed during plastic deformation and the energy J dissipated during microstructure evolution. The relationship among them can be expressed as Eq. (15) [28,47–49]:

$$P = \sigma \cdot \dot{\varepsilon} = G + J = \int_0^{\dot{\varepsilon}} \sigma \mathrm{d}\dot{\varepsilon} + \int_0^{\sigma} \dot{\varepsilon} \mathrm{d}\sigma \tag{15}$$

Prasad [47] defined η as the power dissipation efficiency—this metric is used to construct the energy dissipation map. The term η is related to the energy J and the ideal linear dissipated energy J_{max}, which can be expressed as Eq. (16):

$$\eta = \frac{J}{J_{max}} = \frac{2m}{m+1} \tag{16}$$

where m is the strain rate sensitive parameter, which plays a key role in the whole calculation process. According to flow stress analysis in Section 3.1, the stress is sensitive to changes in strain rate. Under a certain deformation temperature and strain, the relationship between the stress and strain rate can be written as $\sigma = K \cdot \dot{\varepsilon}^m$ and is widely used to describe the constitutive relation. The term m can then be calculated by Eq. (17) [28,47–49]:

$$m = \frac{\partial J}{\partial G} = \frac{\dot{\varepsilon}\mathrm{d}\sigma}{\sigma \mathrm{d}\dot{\varepsilon}} = \frac{\partial \ln \sigma}{\partial \ln \dot{\varepsilon}} \tag{17}$$

The term m is an essential parameter, and the material is in an ideal linear state when $m = 1$, i.e., $J = J_{max} = P/2$. In general, m is between 0 and 1 in a stable flowing viscoplastic solid [50]. The m value in this paper is between 0.1 and 0.3, which is consistent with the range of most steels reported in other literature [51–52]. To reflect the flow instability behavior during deformation, the instability criterion ($\xi(\dot{\varepsilon})$) was established as Eq. (18) [47–49]:

$$\xi(\dot{\varepsilon}) = \frac{\partial \ln\left(\frac{m}{m+1}\right)}{\partial \ln \dot{\varepsilon}} + m < 0 \tag{18}$$

If Eq. (18) is negative, the material flows unsteadily when it deforms under load. According to Eq. (18), the processing map shown in Fig. 11 was obtained by superimposing the instability and energy dissipation maps. The value on the contour line represents the power dissipation coefficient η, and the shaded parts are the instability zone. Fig. 11 shows that instability zones were mainly distributed in a low deformation temperature range of 930–1010°C and a high strain rate range of $\dot{\varepsilon} > 0.1\ s^{-1}$. Under low strains and high deformation temperatures, some small instability zones were also observed. The instability area decreased gradually as strain increased from 0.1 to 0.6.

The new recrystallized grains nucleate and grow at grain boundaries with the increase in deformation temperature. Fig. 9(b) and (d) shows that dynamic recrystallization occurred at lower deformation temperatures. The recrystallized

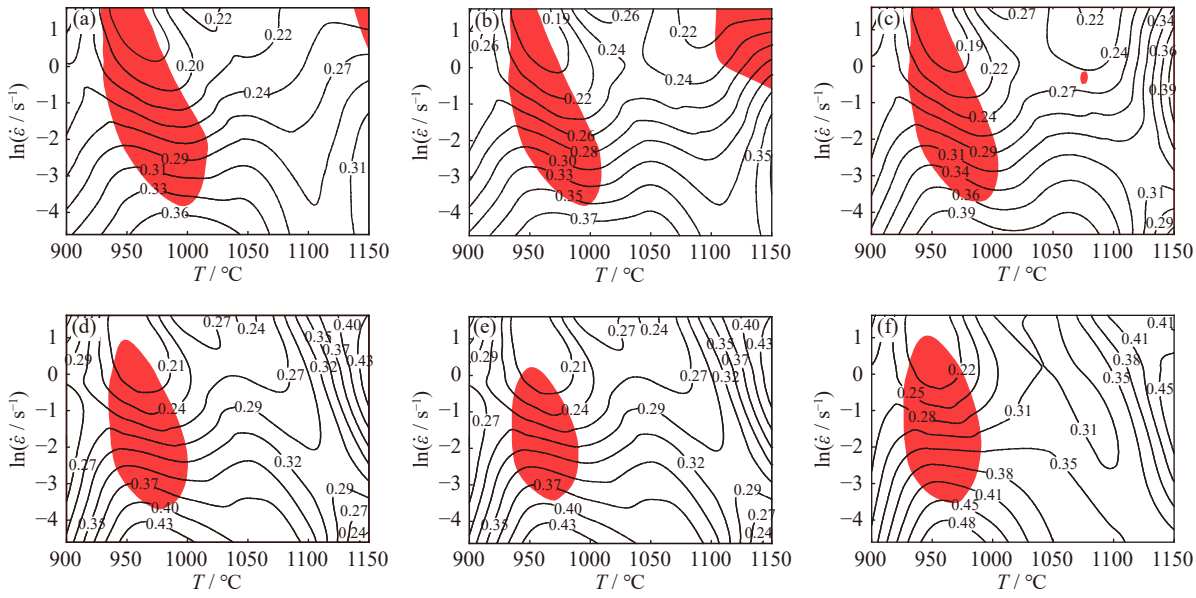

Fig. 11. Processing maps of Fe–27.34Mn–8.63Al–1.03C steel under different true strains: (a) $\varepsilon = 0.1$; (b) $\varepsilon = 0.2$; (c) $\varepsilon = 0.3$; (d) $\varepsilon = 0.4$; (e) $\varepsilon = 0.5$; (f) $\varepsilon = 0.6$.

grains were distributed in a "necklace" structure at the grain boundaries, thus resulting in the flow instability of the tested steel. This corresponded to the shaded areas in Fig. 11 and is due to the inhomogeneous strain distribution between the original austenite grains and the recrystallized austenite grains when the tested steel was deformed. Complete dynamic recrystallization occurred when the deformation temperature exceeded 1050°C. The equiaxed austenite grains were uniformly distributed in the matrix, as shown in Fig. 9(e) and (f). The homogeneous strain distribution during deformation did not lead to flow instability, which corresponds to the stable areas in Fig. 11.

In addition, η reached a peak value at a strain rate of 0.01 s^{-1}. In this case, the instability zones were not observed in Fig. 11, which indicates that the appropriate deformation temperature and sufficient deformation time are the crucial factors driving recrystallization. Therefore, the chosen deformation conditions for the test steel were a temperature range of 1010–1100°C and a strain rate of 0.01 s^{-1} during the hot working process with large deformations. Under these conditions, the tested steel exhibited good hot workability.

4. Conclusions

The stress–strain response of Fe–27.34Mn–8.63Al–1.03C steel was detected in the thermal simulation test. A constitutive equation for thermal compression was established. The main conclusions are as follows.

(1) The activation energy of the test steel was $Q = 422.88$ kJ·mol^{-1}, and the Z equation for the hot compression was $Z = \dot{\varepsilon}\exp[422880/(RT)] = 6.239\times10^{15}\left[\sinh\left(0.0107\sigma_p\right)\right]^{4.24}$.

(2) The relation between peak stress σ_p and critical stress σ_c was expressed by σ_c=0.872σ_p, and the dynamic recrystallization kinetic model followed $X = 1-\exp\left[-0.0467\times\left(\frac{\varepsilon-\varepsilon_c}{\varepsilon_p}\right)^{3.923}\right]$.

(3) The deformation temperature and strain rate had a significant influence on the dynamic recrystallization process. The increase in deformation temperature and the decrease in strain rate could accelerate the occurrence of dynamic recrystallization.

(4) The microstructure and processing map suggested that dynamic recrystallization occurred in regions where η was higher. Therefore, the tested steel exhibited good hot workability with a temperature range of 1010–1100°C and a strain rate of 0.01 s^{-1}.

Acknowledgements

This work was financially supported by the National Natural Science Foundation of China (Nos. 52071300 and 51904278), the Special Funding Projects for Local Science and Technology Development guided by the Central Committee (No. YDZX20191400004587), the Key Research and Development Project of Zhejiang Province, China (No. 2020C01131), and the Innovation projects of colleges and universities in Shanxi Province, China (No. 2019L0577).

Conflict of Interest

To the best of our knowledge, the authors have no conflict of interest, financial, or otherwise.

References

[1] S.P. Chen, R. Rana, A. Haldar, and R.K. Ray, Current state of Fe–Mn–Al–C low density steels, *Prog. Mater. Sci.*, 89(2017), p. 345.

[2] R. Rana, C. Lahaye, and R.K. Ray, Overview of lightweight ferrous materials: Strategies and promises, *JOM*, 66(2014), No. 9, p. 1734.

[3] K. Lu, The future of metals, *Science*, 328(2010), No. 5976, p. 319.

[4] B. Wietbrock, W. Xiong, M. Bambach, and G. Hirt, Effect of temperature, strain rate, manganese and carbon content on flow behavior of three ternary Fe–Mn–C (Fe–Mn23–C0.3, Fe–Mn23–C0.6, Fe–Mn28–C0.3) high-manganese steels, *Steel Res. Int.*, 82(2011), No. 1, p. 63.

[5] H.L. Yi, L. Sun, and X.C. Xiong, Challenges in the formability of the next generation of automotive steel sheets, *Mater. Sci. Technol.*, 34(2018), No. 9, p. 1112.

[6] W. Bleck, New insights into the properties of high-manganese steel, *Int. J. Miner. Metall. Mater.*, 28(2021), No. 5, p. 782.

[7] B.C. de Cooman, Y. Estrin, and S.K. Kim, Twinning-induced plasticity (TWIP) steels, *Acta Mater.*, 142(2018), p. 283.

[8] S.S. Li and H.W. Luo, Medium-Mn steels for hot forming application in the automotive industry, *Int. J. Miner. Metall. Mater.*, 28(2021), No. 5, p. 741.

[9] Y.J. Wang, S. Zhao, R.B. Song, and B. Hu, Hot ductility behavior of a Fe–0.3C–9Mn–2Al medium Mn steel, *Int. J. Miner. Metall. Mater.*, 28(2021), No. 3, p. 422.

[10] J. Hu, J.M. Zhang, G.S. Sun, *et al.*, High strength and ductility combination in nano-/ultrafine-grained medium-Mn steel by tuning the stability of reverted austenite involving intercritical annealing, *J. Mater. Sci.*, 54(2019), No. 8, p. 6565.

[11] J. Hu, L.X. Du, W. Xu, *et al.*, Ensuring combination of strength, ductility and toughness in medium-manganese steel through optimization of nano-scale metastable austenite, *Mater. Charact.*, 136(2018), p. 20.

[12] S.W. Hwang, J.H. Ji, and K.T. Park, Effects of Al addition on high strain rate deformation of fully austenitic high Mn steels, *Mater. Sci. Eng. A*, 528(2011), No. 24, p. 7267.

[13] C.Y. Chao and C.H. Liu, Effects of Mn contents on the microstructure and mechanical properties of the Fe–10Al–*x*Mn–1.0C alloy, *Mater. Trans.*, 43(2002), No. 10, p. 2635.

[14] D. Raabe, H. Springer, I. Gutierrez-Urrutia, *et al.*, Alloy design, combinatorial synthesis, and microstructure–property relations for low-density Fe–Mn–Al–C austenitic steels, *JOM*, 66(2014), No. 9, p. 1845.

[15] I. Kalashnikov, A. Shalkevich, O. Acselrad, and L.C. Pereira, Chemical composition optimization for austenitic steels of the Fe–Mn–Al–C system, *J. Mater. Eng. Perform.*, 9(2000), No. 6, p. 597.

[16] C.M. Chu, H. Huang, P.W. Kao, and D. Gan, Effect of alloying chemistry on the lattice constant of austenitic Fe–Mn–Al–C alloys, *Scripta Metall. Mater.*, 30(1994), No. 4, p. 505.

[17] H. Kim, D.W. Suh, and N.J. Kim, Fe–Al–Mn–C lightweight structural alloys: A review on the microstructures and mechanical properties, *Sci. Technol. Adv. Mater.*, 14(2013), No. 1, art. No. 014205.

[18] A.S. Hamada, L.P. Karjalainen, M.C. Somani, and R.M. Ramadan, Deformation mechanisms in high-Al bearing high-Mn TWIP steels in hot compression and in tension at low temperatures, *Mater. Sci. Forum*, 550(2007), p. 217.
[19] R. Rana, C. Liu, and R.K. Ray, Evolution of microstructure and mechanical properties during thermomechanical processing of a low-density multiphase steel for automotive application, *Acta Mater.*, 75(2014), p. 227.
[20] C. Haase, C. Zehnder, T. Ingendahl, *et al*., On the deformation behavior of κ-carbide-free and κ-carbide-containing high-Mn light-weight steel, *Acta Mater.*, 122(2017), p. 332.
[21] Y.H. Mozumder, K. Babu, R. Saha, and S. Mandal, Deformation mechanism and nano-scale interplay of dual precipitation during compressive deformation of a duplex lightweight steel at high strain rate, *Mater. Sci. Eng. A*, 823(2021), art. No. 141725.
[22] R.W.K. Honeycombe and R.W. Pethen, Dynamic recrystallization, *J. Less Common Met*., 28(1972), No. 2, p. 201.
[23] T.K. Sakai, A. Belyakov, R. Kaibyshev, H. Miura, and J.J. Jonas, Dynamic and post-dynamic recrystallization under hot, cold and severe plastic deformation conditions, *Prog. Mater. Sci.*, 60(2014), p. 130.
[24] H.R. Abedi, A.Z. Hanzaki, Z. Liu, R. Xin, N. Haghdadi, and P.D. Hodgson, Continuous dynamic recrystallization in low density steel, *Mater. Des.*, 114(2017), p. 55.
[25] L.X. Xu, H.B. Wu, and X.T. Wang, Influence of microstructural evolution on the hot deformation behavior of an Fe–Mn–Al duplex lightweight steel, *Acta Metall. Sinica Engl. Lett.*, 31(2018), No. 4, p. 389.
[26] D.G. Liu, H. Ding, X. Hu, D. Han, and M.H. Cai, Dynamic recrystallization and precipitation behaviors during hot deformation of a κ-carbide-bearing multiphase Fe–11Mn–10Al–0.9C lightweight steel, *Mater. Sci. Eng. A*, 772(2020), art. No. 138682.
[27] D.T. Pierce, D.M. Field, K.R. Limmer, T. Muth, and K.M. Sebeck, Hot deformation behavior of an industrially cast large grained low density austenitic steel, *Mater. Sci. Eng. A*, 825(2021), art. No. 141785.
[28] J. Sun, J.H. Li, P. Wang, and Z.Y. Huang, Hot deformation behavior, dynamic recrystallization and processing map of Fe–30Mn–10Al–1C low-density steel, *Trans. Indian Inst. Met.*, 75(2022), No. 3, p. 699.
[29] L. Duprez, B.C. De Cooman, and N. Akdut, Flow stress and ductility of duplex stainless steel during high-temperature torsion deformation, *Metall. Mater. Trans. A*, 33(2002), No. 7, p. 1931.
[30] F. Montheillet, Moving grain boundaries during hot deformation of metals: Dynamic recrystallization, [in] F.D. Fischer, ed., *Moving Interfaces in Crystalline Solids*, CISM International Centre for Mechanical Sciences, Vol. 453, Springer, Vienna, 2004, p. 203.
[31] C. Zener and J.H. Hollomon, Effect of strain rate upon plastic flow of steel, *J. Appl. Phys.*, 15(1944), No. 1, p. 22.
[32] Y.S. Li, Y.W. Dong, Z.H. Jiang, Q.F. Tang, S.Y. Du, and Z.W. Hou, Influence of rare earth Ce on hot deformation behavior of as-cast Mn18Cr18N high nitrogen austenitic stainless steel, *Int. J. Miner. Metall. Mater.*, 30(2023), No. 2, p. p.
[33] C.M. Sellars and W.J. McTegart, On the mechanism of hot deformation, *Acta Metall.*, 14(1966), No. 9, p. 1136.
[34] Y.P. Li, R.B. Song, E.D. Wen, and F.Q. Yang, Hot deformation and dynamic recrystallization behavior of austenite-based low-density Fe–Mn–Al–C steel, *Acta Metall. Sinica Engl. Lett.*, 29(2016), No. 5, p. 441.
[35] O.A. Zambrano, J. Valdés, Y. Aguilar, J.J. Coronado, S.A. Rodríguez, and R.E. Logé, Hot deformation of a Fe–Mn–Al–C steel susceptible of κ-carbide precipitation, *Mater. Sci. Eng. A*, 689(2017), p. 269.
[36] A. Khosravifard, A.S. Hamada, M.M. Moshksar, R. Ebrahimi, D.A. Porter, and L.P. Karjalainen, High temperature deformation behavior of two as-cast high-manganese TWIP steels, *Mater. Sci. Eng. A*, 582(2013), p. 15.
[37] A.S. Hamada, L.P. Karjalainen, and M.C. Somani, The influence of aluminum on hot deformation behavior and tensile properties of high-Mn TWIP steels, *Mater. Sci. Eng. A*, 467(2007), No. 1-2, p. 114.
[38] Z.Q. Wu, Y.B. Tang, W. Chen, *et al*., Exploring the influence of Al content on the hot deformation behavior of Fe–Mn–Al–C steels through 3D processing map, *Vacuum*, 159(2019), p. 447.
[39] H. Mirzadeh, J.M. Cabrera, J.M. Prado, and A. Najafizadeh, Hot deformation behavior of a medium carbon microalloyed steel, *Mater. Sci. Eng. A*, 528(2011), No. 10-11, p. 3876.
[40] E.I. Poliak and J.J. Jonas, A one-parameter approach to determining the critical conditions for the initiation of dynamic recrystallization, *Acta Mater.*, 44(1996), No. 1, p. 127.
[41] G.M. Liu, J.B. Wang, Y.F. Ji, *et al*., Hot deformation behavior and microstructure evolution of Fe–5Mn–3Al–0.1C high-strength lightweight steel for automobiles, *Materials*, 14(2021), No. 10, art. No. 2478.
[42] S. Mandal, M. Jayalakshmi, A.K. Bhaduri, and V.S. Sarma, Effect of strain rate on the dynamic recrystallization behavior in a nitrogen-enhanced 316L(N), *Metall. Mater. Trans. A*, 45(2014), No. 12, p. 5645.
[43] J.J. Jonas, X. Quelennec, L. Jiang, and É. Martin, The Avrami kinetics of dynamic recrystallization, *Acta Mater.*, 57(2009), No. 9, p. 2748.
[44] Z.Y. Huang, Y.S. Jiang, A.L. Hou, *et al*., Rietveld refinement, microstructure and high-temperature oxidation characteristics of low-density high manganese steels, *J. Mater. Sci. Technol.*, 33(2017), No. 12, p. 1531.
[45] M. Shaban and B. Eghbali, Determination of critical conditions for dynamic recrystallization of a microalloyed steel, *Mater. Sci. Eng. A*, 527(2010), No. 16-17, p. 4320.
[46] Y.V.R.K. Prasad, H.L. Gegel, S.M. Doraivelu, *et al*., Modeling of dynamic material behavior in hot deformation: Forging of Ti-6242, *Metall. Trans. A*, 15(1984), No. 10, p. 1883.
[47] Y.V.R.K. Prasad, Processing maps: A status report, *J. Mater. Eng. Perform.*, 12(2003), No. 6, p. 638.
[48] P. Wan, H.X. Yu, F. Li, P.F. Gao, L. Zhang, and Z.Z. Zhao, Hot deformation behaviors and process parameters optimization of low-density high-strength Fe–Mn–Al–C alloy steel, *Met. Mater. Int.*, 28(2022), No. 10, p. 2498.
[49] M.S. Ghazani and B. Eghbali, Strain hardening behavior, strain rate sensitivity and hot deformation maps of AISI 321 austenitic stainless steel, *Int. J. Miner. Metall. Mater.*, 28(2021), No. 11, p. 1799.
[50] H. Ziegler, Some extremum principles in irreversible thermodynamics, with application to continuum mechanics, *Prog. Solid Mech.*, 4(1963), p. 93.
[51] A. Momeni and K. Dehghani, Hot working behavior of 2205 austenite–ferrite duplex stainless steel characterized by constitutive equations and processing maps, *Mater. Sci. Eng. A*, 528(2011), No. 3, p. 1448.
[52] M.A. Davinci, D. Samantaray, U. Borah, S.K. Albert, and A.K. Bhaduri, Influence of processing parameters on hot workability and microstructural evolution in a carbon-manganese-silicon steel, *Mater. Des.*, 88(2015), p. 567.